Computational Materials Science 187 (2021) 110123

Contents lists available at ScienceDirect

Computational Materials Science

journal homepage: www.elsevier.com/locate/commatsci

Three-dimensional Phase-field simulation of γ'' precipitation kinetics in Inconel 625 during heat treatment

Caleb O. Yenusah [a,b,1], Yanzhou Ji [c,1], Yucheng Liu [a,b,*], Tonya W. Stone [a,b], Mark F. Horstemeyer [d], Long-Qing Chen [c], Lei Chen [e,*]

[a] Department of Mechanical Engineering, Mississippi State University, Mississippi State, MS 39762, USA
[b] Center for Advanced Vehicular Systems, Mississippi State University, Mississippi State, MS 39762, USA
[c] Department of Materials Science and Engineering, The Pennsylvania State University, University Park, PA 16801 USA
[d] School of Engineering, Liberty University, Lynchburg, VA 24515, USA
[e] Department of Mechanical Engineering, University of Michigan-Dearborn, Dearborn, MI 48128, USA

ARTICLE INFO

Keywords:
Phase-field model
Precipitation kinetics
Non-isothermal aging
Nickel-base alloys
Precipitation strengthening
γ''

ABSTRACT

Metastable γ'' ($D0_{22}$-Ni_3Nb) particles are strengthening precipitates for commercial Inconel 625 Ni-based superalloy. Understanding their morphological evolution is critical for evaluating its hardening effects and guiding heat treatments to improve its yield strength. Here we present a phase-field model to model and analyze the nucleation and growth kinetics of metastable γ'' in Inconel 625 during isothermal and non-isothermal aging conditions with thermodynamic properties, diffusion coefficients, and misfit strain data from both the literature and calibration to experimental results. We implemented the classical nucleation theory to introduce local nucleation taking into account local supersaturation. The simulated mean particle length and aspect ratio are in agreement with experimental data at 600 °C and 650 °C during isothermal aging. Utilizing the phase-field simulation results as input parameters, the coherency strengthening effect of γ'' as a function of aging temperature and time is predicted. A multistage aging strategy to optimize the γ'' strengthening effect and to reduce aging times using the developed phase-field model and coherency strengthening model is suggested.

1. Introduction

Inconel 625 is widely used in the aerospace, chemical processing, power, and marine industries, due to its high strength, outstanding fatigue, corrosion, and oxidation resistance, and excellent fabricability and weldability [1]. Inconel 625 was originally designed as a solid-solution strengthened alloy but was found to be highly susceptible to precipitation hardening by the formation of the body-centered tetragonal (BCT) γ'' phase ($D0_{22}$-Ni_3Nb) after thermal aging between 550 °C and 750 °C [1,2,3]. Aging controls the size distribution, volume fraction, and morphology of the γ'' precipitates, which in turn determines the mechanical properties of the alloy. Therefore, understanding the morphological evolution of γ'' during aging is critical for evaluating their hardening effects and improving the mechanical properties of the alloy.

Numerical investigation of the process-structure–property relationship in materials is becoming increasingly attractive because of the time and cost-saving it can potentially offer [4,5]. This is especially true for Inconel 625 that requires hundreds or even thousands of hours of aging time to achieve a significant precipitation-hardening effect [3,6,7]. Therefore, theoretical analysis or computer simulation is a promising complement to trial-and-error-based experiments in optimizing the heat treatment strategy. Using the Svoboda-Fischer-Fratzl-Kozeschnik (SFFK) and subsequently, Lifshitz-Slyozov-Encounter-Modified (LSEM) frameworks, Moore *et al.* [8,9] were able to capture γ'' evolution trends during heat treatment. The major drawback of these frameworks is that since γ'' exhibits a plate-shaped morphology, the model parameters have to be calibrated to experimentally measured aspect ratio data at all temperatures and times of interest, which is a laborious undertaking.

The physics-based phase-field method [10], which introduces the diffuse-interface concept to avoid the explicit tracking of interfaces, stands out with the significant potential to accurately predict precipitate morphology, growth, and coarsening kinetics in various alloy systems. Notable examples of its application include: γ' and γ'' precipitates in Ni-alloys [11,12,13,14], β' and β_1 precipitates in Mg-rare earth alloys

* Corresponding authors.
E-mail addresses: liu@me.msstate.edu (Y. Liu), leichn@umich.edu (L. Chen).
[1] These authors contributed equally.

https://doi.org/10.1016/j.commatsci.2020.110123
Received 11 June 2020; Received in revised form 13 October 2020; Accepted 14 October 2020

Table 1
Composition (at.%) of Inconel 625 [9].

Ni	Cr	Fe	Mo	Nb	C	Mn	Si	P	S	Al	Ti
63.05	24.85	3.05	5.32	2.43	0.10	0.22	0.49	0.02	0.01	0.26	0.20

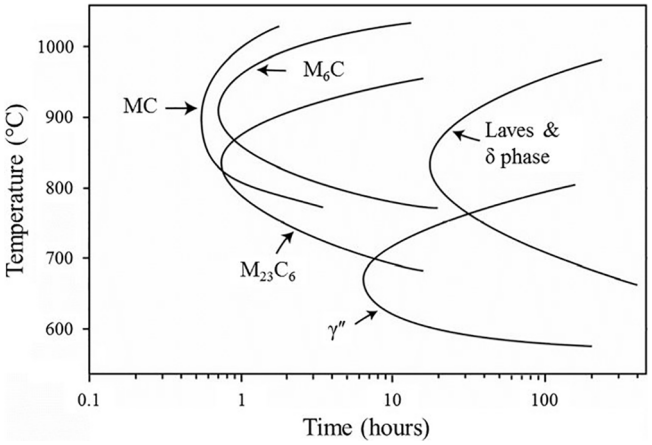

Fig. 1. Time-Temperature-Transformation (TTT) diagram for Inconel 625. Adapted from Floreen *et al.* [2].

[15,16,17] , θ' precipitates in Al-Cu-based alloys [18,19,20], and α precipitates in Ti-alloys [21]. The phase-field model offers two main advantages for simulating the morphological evolution of γ'' over the SFFK and LSEM models. Firstly, because the lattice misfit strain between the precipitate (γ'') and the matrix (γ) serves as input for the phase-field model, the model can accurately predict γ'' aspect ratio evolution, eliminating the need to calibrate to experimentally observed aspect ratio evolution data. Secondly, since the phase-field model captures the growth of particles under elastic stresses [22] and compositional strains [23], the "directional encounter" phenomenon observed in γ'' precipitates [9] is naturally captured by the model. The phase-field method has been used to study γ'' precipitation kinetics in nickel-based superalloys. For example, Zhou *et al.* [13] studied γ', γ'', and δ precipitation in Inconel 718. Shi *et al.* [24] investigated the growth behavior of γ'/γ'' coprecipitates in nickel-base superalloys. Ji *et al.* [14] studied the coherency loss of γ'' in Inconel 718. However, these existing investigations either exclusively focused on the growth behavior of particles without careful consideration of nucleation kinetics, or lacked comprehensive experimental validations in terms of γ'' mean size, volume fraction, and morphology evolution, all of which are necessary prerequisites for a reliable and predictive computational model of γ'' precipitate kinetics and the resultant strengthening effects.

The aim of this study is to develop a phase-field model for predicting the precipitation kinetics and morphology evolution of γ'' precipitates in Inconel 625 during isothermal and non-isothermal aging conditions. To obtain more quantitative simulation results, we incorporate nucleation and more accurate diffusion-controlled kinetics to the phase-field model developed by Zhou *et al.* [13]. All input parameters are taken from validated experimental measurements, theoretical calculations, or calibration to experimental results. The implemented explicit nucleation method based on the classical nucleation theory enables us to capture the spatial distribution of nuclei as a function of local supersaturation. The simulation results for mean particle size, aspect-ratio, and volume fraction evolution are in agreement with the experimental data for simulations at 600 °C and 650 °C during isothermal aging. Utilizing the results from the phase-field simulations as input parameters to a macroscale coherency strengthening model, the coherency strengthening effect of γ'' as a function of aging temperature and time is predicted. Finally, a multistage aging strategy to optimize hardening effects and reduce aging time by utilizing the developed phase-field model and coherency strengthening model is discussed.

2. Methodology

Inconel 625 is a multi-component alloy with about twelve or more components. The typical alloying elements in Inconel 625 and their compositions are shown in Table 1. The main phases appearing in Inconel 625 during thermal aging are γ'', δ, Laves, MC, M_6C, and $M_{23}C_6$ carbides as shown in the Time-Temperature-Transformation (TTT) diagram in Fig. 1. Inconel 625 does not precipitate the $L1_2$-ordered γ' phase found in most nickel-base superalloys (e.g. Inconel 718) because of its low aluminum and titanium contents. Only the strengthening γ'' phase is considered in this work because of the ageing time, temperatures and the focus on intragranular precipitation in this study.

To save computational efforts while capturing the essential features of the precipitation process, we used a pseudo-ternary (Ni-Al_x-Nb_y) CALPHAD thermodynamic database developed for Ni-based superalloys [25]. This database considers Al_x as a weighted summation of all γ'-forming elements (Al and Ti) and Nb_y as weighted summation of all γ''- and δ-forming elements (Nb and Ta), which will be represented by Al* and Nb*, respectively. The system is represented with two composition fields, X_{Al^*} and X_{Nb^*}. As γ'' is a tetragonal phase embedded in the cubic γ matrix and exhibits an orientation relationship of $\{1\,0\,0\}_{\gamma''}//\{1\,0\,0\}_{\gamma}$ and $[0\,0\,1]_{\gamma''}//\langle 1\,0\,0\rangle_{\gamma}$, three orientation variants with different $\{1\,0\,0\}$ habit planes will appear. Therefore, all three orientation variants of γ'' were considered in the 3D phase-field simulations, with two antiphase domains introduced for each γ'' variant. The existence of the antiphase domains will reduce the frequency of coalescence events between the same variant during the growth and coarsening stages. Therefore, γ'' is represented by three order parameters, $\{\eta_1, \eta_2, \eta_3\}$ to represent the three variants $\{\pm1,0,0\},\{0,\pm1,0\},\{0,0,\pm1\}$, where the two antiphase domains of the same variant are represented by $+1$ and -1, respectively. With this definition, $|\eta_p| = 0$ corresponds to the matrix phase and $0 < |\eta_p| < 1$ corresponds to the γ/γ'' interface. In order to simulate both isothermal and non-isothermal aging conditions, the temperature dependent total free energy functional for the single crystal system can then be expressed as:

$$F = \int_V \left[f_{bulk}\left(X_{Al^*}, X_{Nb^*}, \eta_p, T\right) + f_{grad}\left(\nabla\eta_p\right) + e_{el} \right] dV \tag{1}$$

where f_{bulk} is the bulk free energy density of the system, f_{grad} is the gradient energy due to inhomogeneous distribution of the order parameters, and e_{el} is the elastic strain energy density.

$$f_{bulk}\left(X_{Al^*}, X_{Nb^*}, \{\eta_p\}, T\right) = V_m^{-1}\cdot\left[1 - \sum_{p=1}^{3} h(\eta_p)\right]\cdot f^{\gamma}\left(X^{\gamma}_{Al^*}, X^{\gamma}_{Nb^*}, T\right) + V_m^{-1}\cdot\sum\nolimits_{p=1}^{3} h(\eta_p)\cdot f^{\gamma''}\left(X^{\gamma''}_{Al^*}, X^{\gamma''}_{Nb^*}, T\right) + g(\{\eta_p\}) \tag{2}$$

2.1. Bulk free energy

The bulk free energy of the system is the sum of the Gibbs free energy of different phases and the energy variation due to structural change and is expressed as the following,

where $f^{\gamma}\left(X^{\gamma}_{Al^*}, X^{\gamma}_{Nb^*}, T\right)$ and $f^{\gamma''}\left(X^{\gamma''}_{Al^*}, X^{\gamma''}_{Nb^*}, T\right)$ are the molar Gibbs free energy of γ and γ'' phases, obtained from the pseudo-ternary thermodynamic database [25]. V_m is the molar volume, $h(\eta_p)$ is an interpolation function, and $g(\{\eta_p\})$ is the sum of a triple well and interaction energy functions. The expressions for $h(\eta_p)$ and $g(\{\eta_p\})$ are given by the following,

$$h(\eta_p) = 2\eta_p^2 - \eta_p^4 \tag{3}$$

$$g(\{\eta_p\}) = w^{\gamma''}\cdot\sum_{p=1}^{3}\eta_p^2\left(1-|\eta_p|\right)^2 + \alpha\cdot\sum_{p=1}^{3}\sum_{p\neq q}^{3}\eta_p^2\eta_q^2 \tag{4}$$

where $w^{\gamma''}$ defines the free energy hump between the matrix and the precipitate phase. The second term in Eq. (4) describes the free energy penalty that prevents different γ'' variants from occupying the same spatial position and α is a constant parameter which determines the magnitude of the penalty. It is worth noting that the triple well function (first term in Eq. (4)) leads to wetting of matrix phase at antiphase boundaries. To incorporate the physical antiphase domains, additional order parameters can be defined and evolved for each type of antiphase domains [26]. However, since the total volume fraction of γ'' in the present study is quite small (<7%), the current treatment of antiphase boundaries will not lead to significant changes compared to simulations with or without considering the physical antiphase domains. This is because, the small volume fraction would not lead to significant particle coalescence where antiphase domains may play more important roles in precipitation kinetics.

The Kim-Kim-Suzuki (KKS) model [27] is employed to remove the extra double-well potential of composition due to the equal composition assumption at interfaces [28,29]. It assumes local equilibrium with equal diffusion chemical potential, rather than equal composition, at interfaces. This requires the solution of concentration fields in each phase from the following equations,

$$X_i = X_i^{\gamma}\cdot\left[1-\sum_{p=1}^{3}h(\eta_p)\right] + X_i^{\gamma''}\cdot\sum_{p=1}^{3}h(\eta_p),\ \ i = Al^*, Nb^* \tag{5a}$$

$$\frac{\partial f^{\gamma}}{\partial X_i^{\gamma}} = \frac{\partial f^{\gamma''}}{\partial X_i^{\gamma''}},\ \ i = Al^*, Nb^* \tag{5b}$$

The non-linear molar Gibbs free energies of f^{γ} and $f^{\gamma''}$ were approximated by Taylor series expansions at equilibrium compositions up to 2nd order as:

$$\begin{aligned} f^{\theta}_{para}\left(X^{\theta}_{Al^*}, X^{\theta}_{Nb^*}, T\right) &= A^{\theta} + B^{\theta}_{Al^*}\left(X^{\theta}_{Al^*} - X^{\theta,eq}_{Al^*}\right) + B^{\theta}_{Nb^*}\left(X^{\theta}_{Nb^*} - X^{\theta,eq}_{Nb^*}\right) \\ &+\frac{1}{2}C^{\theta}_{Al^*,Al^*}\left(X^{\theta}_{Al^*} - X^{\theta,eq}_{Al^*}\right)^2 + C^{\theta}_{Al^*,Nb^*}\left(X^{\theta}_{Al^*} - X^{\theta,eq}_{Al^*}\right)\left(X^{\theta}_{Nb^*} - X^{\theta,eq}_{Nb^*}\right) \\ &+\frac{1}{2}C^{\theta}_{Nb^*,Nb^*}\left(X^{\theta}_{Nb^*} - X^{\theta,eq}_{Nb^*}\right)^2, \theta = \gamma, \gamma'' \end{aligned} \tag{6}$$

where $f^{\theta}_{para}\left(X^{\theta}_{Al^*}, X^{\theta}_{Nb^*}, T\right)$ is the parabolic approximation of $f^{\theta}\left(X^{\theta}_{Al^*}, X^{\theta}_{Nb^*}, T\right)$. The temperature dependent equilibrium compositions of Al* and Nb* in phase θ are $X^{\theta,eq}_{Al}$ and $X^{\theta,eq}_{Nb}$, respectively. The constants A^{θ}, $B^{\theta}_{Al^*}$, $B^{\theta}_{Nb^*}$, $C^{\theta}_{Al^*,Al^*}$, $C^{\theta}_{Al^*,Nb^*}$, and $C^{\theta}_{Nb^*,Nb^*}$ are temperature dependent Taylor expansion coefficients which are calculated from the Ni-Al_x-Nb_y pseudo-ternary database [25] as follows:

$$A^{\theta} = f^{\theta}(X^{\theta,eq}_{Al^*}, X^{\theta,eq}_{Nb^*}, T) \tag{7a}$$

Table 2
Expressions for parameters in the nucleation model (Eq. (12)) [56].

Parameters	Description	Expression
$Z[dim.less]$	Zeldovich factor	$\frac{a^3\Delta G_c^2}{8\pi\sqrt{\kappa_B T\sigma^3}}$
$\beta^*[s^{-1}]$	Atomic attachment rate	$\frac{4\pi r_c^2}{a^4}\left[\sum_{i=1}^{n}\frac{(X_{ki}-X_{0i})^2}{X_{0i}D_{0i}}\right]^{-1}$
$r_c[m]$	Critical radius	$-\frac{2\sigma}{\Delta G_c}$
$\Delta G^*[J]$	Critical nucleation energy	$\frac{16\pi}{3}\frac{\sigma^3}{\Delta G_c^2}$
$\Delta G_c[J\cdot m^{-3}]$	Nucleation driving force	$\frac{1}{V_m}\sum_{i=1}^{n}X_{ki}(\mu_{ki}-\mu_{0i})$
$\tau[s]$	Incubation time	$\tau = \frac{1}{2\beta^* Z^2}$

Where a is matrix atomic distance; k_B is Boltzmann's constant; T is temperature; X_{ki}/X_{0i} is the element compositions in precipitate/matrix; D_{0i} is diffusivities in matrix; and σ is interfacial energy.

$$B_i^{\theta} = \left.\frac{\partial f^{\theta}}{\partial X_i^{\theta}}\right|_{X_i^{\theta}=X_i^{\theta,eq}}, i = Al^*, Nb^* \tag{7b}$$

$$C_{i,j}^{\theta} = \left.\frac{\partial f^{\theta}}{\partial X_i^{\theta}}\right|_{X_i^{\theta}=X_i^{\theta,eq}}, i,j = Al^*, Nb^* \tag{7c}$$

Therefore, the first derivatives of the free energies with respect to concentrations in Eq. (5b) are linear functions of the concentrations. Hence, Eqs. (5a) and (5b) can be solved analytically through matrix inversions [14].

2.2. Gradient energy

The gradient energy describes the energy penalty due to the inhomogeneous distribution of phase-field variables near interfaces expressed as the following,

$$f_{grad} = \sum_{p=1}^{3}\frac{\kappa_p}{2}(\nabla\eta_p)^2 \tag{8}$$

where κ_p is the gradient energy coefficient which together with the barrier height $w^{\gamma''}$ in Eq. (4), can be obtained from the interfacial energy (σ) and interface thickness (2λ) according to the following relationships [27]:

$$\sigma = \frac{\sqrt{\kappa\cdot w}}{3\sqrt{2}} \tag{9a}$$

$$(2\lambda) = 2.2\sqrt{2}\cdot\sqrt{\frac{\kappa}{w}} \tag{9b}$$

2.3. Elastic strain energy

The elastic strain energy contribution due to lattice misfit between the precipitate and the matrix is evaluated by Khachaturyan's microelasticity theory [30],

$$e_{el} = \frac{1}{2}C_{ijkl}\left(\epsilon_{ij} - \epsilon_{ij}^0\right)\left(\epsilon_{kl} - \epsilon_{kl}^0\right) \tag{10}$$

where C_{ijkl} are elastic constants, ϵ_{ij}^0 is the stress-free transformation strain tensor between the precipitate (γ'') and the matrix (γ). The total strain ϵ_{ij} is calculated from the stress equilibrium equation at each simulation time step. We assume a homogeneous elastic modulus [31] (i.e. the precipitate and matrix phases are assumed to have the same elastic constants) and that stress equilibrium is reached much faster than the diffusional phase transformation.

2.4. Nucleation

Nucleation is incorporated into the phase-field model using the method described by Simmons *et al.* [32,33]. The probability for nucleation at a simulation cell is defined by the following,

$$P = 1 - exp(-J\cdot\Delta t) \tag{11}$$

where Δt is the time step and J is the nucleation rate, which, following the classical nucleation theory of Johnson-Mehl-Avrami-Kolmogorov [34,35,36], is expressed as the following,

$$J = Z\beta^* N_0 exp\left(\frac{-\Delta G^*}{k_B T}\right) exp\left(\frac{-\tau}{t}\right) \tag{12}$$

here Z is Zeldovich's factor, β^* is atomic attachment rate, N_0 is the number of available nucleation sites in the system, ΔG^* is the nucleation barrier, k_B is Boltzmann's constant, T is temperature, τ is the incubation time for nucleation, and t is elapsed time. These quantities can be calculated from the expressions given in Table 2.

At the beginning of the simulations when no precipitate has nucleated in the simulation volume, all grid points are possible nucleation sites. Therefore, the nucleation probability is computed at all grid points. As precipitates nucleate and grow, the grid points occupied by the precipitates (i.e., $|\eta_p| > 0.5$) are excluded from the possible nucleation cites. Therefore, the nucleation probability is only computed for grid points that are not occupied by precipitates (i.e., $|\eta_p| < 0.5$). During nucleation, the nuclei are assumed to be spherical and γ'' variants are randomly selected. The composition of the critical nuclei at a given temperature is set to the equilibrium composition $\left(X^{\gamma'',eq}_{Nb^*}, X^{\gamma'',eq}_{Al^*}\right)$ calculated from the thermodynamic database [25]. Since γ'' is rich in Nb*, the composition of Nb* was radially reduced in the matrix phase around the nucleus $(|\eta_p| < 0.1)$ by exactly the amount required to give the additional solute necessary for the γ'' nucleus. The concentration of Nb* in the depleted region is set to the equilibrium of Nb* in the matrix ($X^{\gamma,eq}_{Nb^*}$). Conversely, since γ'' is Al* poor, the composition of Al* in the matrix is enriched up to the equilibrium concentration ($X^{\gamma,eq}_{Al^*}$) to accommodate for the reduction of Al* in the γ'' nucleus. The critical radii of γ'' nuclei were at least three grid points ($3l_0$) to ensure that the nucleating particles are stable. Note that the described seeding method does not satisfy diffusion at the instance of particle nucleation because the initial depleted/enriched layer around the nucleus are sharp. Subsequent simulation time steps will diffuse these boundaries to satisfy Eq. (13a). Although a nucleation algorithm that naturally satisfies diffusion is available [37], the hold time required to obtain a stable nucleus is too lengthy because of the slow growth kinetics of γ'' investigated in this study which would increase the computational effort needed to introduce each nuclei.

2.5. Kinetic equations

The diffusion and Allen-Cahn [38] equations are solved to obtain the spatial and temporal evolution of the concentration fields and order parameters, respectively,

$$\frac{\partial X_i}{\partial t} = \nabla\cdot\left(M_i\nabla\frac{\partial f^\gamma}{\partial X_i^\gamma}\right), i = Al^*, Nb^* \tag{13a}$$

$$\frac{\partial \eta_p}{\partial t} = -L\left(\frac{\partial f_{bulk}}{\partial \eta_p} - \kappa_p\nabla^2\eta_p + \frac{\partial e_{el}}{\partial \eta_p}\right) \tag{13b}$$

where $M_i (i = Al^*, Nb^*)$ are the chemical mobilities of Al^* and Nb^*, respectively. The mobilities can be estimated as $M_i = \frac{D_i}{V_m\frac{\partial^2 f^\gamma}{\partial X_i^2}}$, where $D_i = D_0 exp\left(\frac{-Q_d}{RT}\right)\left(i = Al^*, Nb^*\right)$ are the temperature dependent diffusivities of Al^* and Nb^*. L is the kinetic coefficient for structural evolution. The value of L is selected to ensure diffusion-controlled growth of the precipitates. These governing equations are normalized by the simulation grid size l_0 and a reference energy density E_0 and were solved numerically using the spectral method proposed by Chen and Shen [39]. The spectral method offers the advantage of accurate simulation results with fewer interfacial grid points compared to discrete methods like the finite difference [39]. The grid size, $l_0 = 0.75nm$ and discretization time step size, $\Delta t^* = 0.01$ were used for all simulations. Real time step can be calculated as:

$$\Delta t = \frac{(l_0)^2\cdot\Delta t^*}{D_{Nb^*}} \tag{14}$$

To provide a sense of the computational times in this work, isothermal aging simulations at 600 ℃ were iterated for 690,000 time-steps and took approximately 48 h. Isothermal aging at 650 ℃ and all multistage aging simulations were iterated for 1,530,000 time-steps, and each took 96 h. All simulations where performed on 20 Intel Xeon CPUs E5-2680 at 2.80 GHz with OpenMP parallel Fortran Codes.

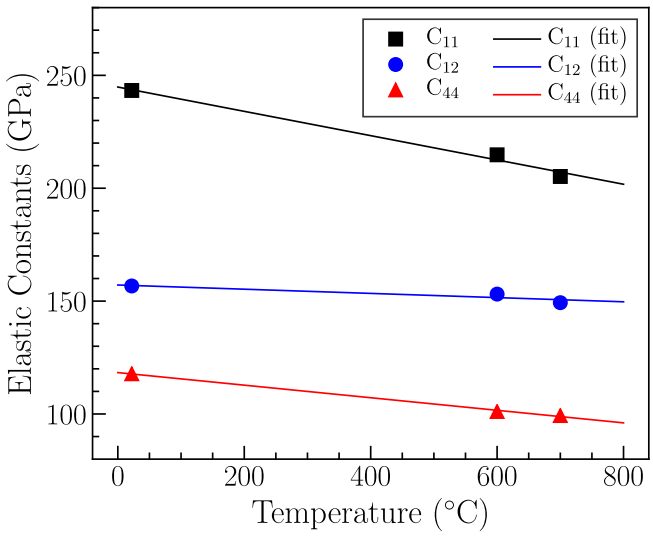

Fig. 2. Elastic constants for γ phase in Inconel 625. Experimental data are sourced from Wang et al. [40] and a linear fit is employed to describe the temperature dependency of the elastic constants.

2.6. Parameterization

This section aims to explain the procedure for model parameter selection. Ideally, little to no calibration of model parameters are needed, since all the parameters in the phase-field model described in Section 2 have physical meaning, and can be obtained from thermodynamic, lower length scale calculations, or experimental measurements. However, given the sensitivity of the simulation results to the interfacial energy, diffusivity, misfit strain, and the scarcity of data for the aforementioned parameters for Inconel 625 in the literature, we conducted preliminary phase-field simulations to identify parameters that best fit the experimental mean particle size and aspect ratio evolution.

To calculate the elastic energy of the system, the elastic constants and misfit strains are needed. The temperature dependent elastic constants data for Inconel 625 was taken from Wang et al. [40] and a linear fit is employed as shown in Fig. 2. Therefore, only the misfit strains are left to be determined for the elastic energy description. Varying misfit strains have been reported for various γ'' precipitating nickel-based super alloys [41,42,43,44,45]. The investigation by Schleifer et al. [31] reported that for $\epsilon^0_{33}/\epsilon^0_{11} \geq 3$, ϵ^0_{33} dictates the plateau aspect ratio. Phase-field aging simulations at 650 ℃ identified $\epsilon^0_{11} = \epsilon^0_{22} = 0.0094$

Table 3
Literature values for the interfacial energy and misfit strain of γ'' precipitates, as well as activation energies for atomic diffusion in nickel-based alloys compared to the values used in this study.

Source	System	Interfacial Energy (mJ/m^2)	$\epsilon^0_{11} = \epsilon^0_{22}(10^{-2})$	$\epsilon^0_{33}(10^{-2})$	Activation Energy (kJ·mol^{-1})
Devaux *et al.* [43]	Inconel 718	95 ± 17	0.67	2.86	272
Cozar *et al.* [44] (25 °C)	Fe 30.8-Ni 9.1-Ta	145	0.94 ± 0.03	3.72 ± 0.06	–
Cozar *et al.* [44] (750 °C)	Fe 30.8-Ni 9.1-Ta	185	0.70	3.46	–
This Study	Inconel 625	172.88 at 600 °C 151.56 at 650 °C	0.94	3.72	295

Table 4
Parameters for phase-field simulations.

Parameters	Description	Expression
V_m	Molar volume	$1.07 \times 10^{-5} m^3/mol$
$X^0_{Al^*}, X^0_{Nb^*}$	Al*, Nb* initial matrix composition	0.0046, 0.0243[9]
D_{0Al^*}, D_{0Nb^*}	Al*, Nb* diffusion prefactor	$8.8 \times 10^{-5} m^2/s$[43]
Q_{Al^*}, Q_{Nb^*}	Al*, Nb* diffusion activation energies	$325 kJmol^{-1}, 295 kJmol^{-1}$
σ	Interfacial energy	$(-0.4264T + 428.72)\frac{mJ}{m^2}$, $600^\circ C \leq T \leq 760^\circ C$
l_0	Simulation grid size	$0.75nm$
E_0	Reference energy density	$2.5GPa$
(2λ)	Interface thickness	$2l_0$
L	Kinetic coefficient	$\frac{L^* D}{E_0 l_0^2}, L^* = 10$ for all T
C_{11}, C_{12}, C_{44}	Elastic constants	$C_{11} = (-0.05383T + 244.8)GPa$, $C_{12} = (-0.009304T + 157.1)GPa$, [40] $C_{44} = (-0.02784T + 118.3)GPa$
ϵ^0_{ij}	Misfit strain tensor	$\begin{bmatrix} 0.0094 & 0 & 0 \\ 0 & 0.0094 & 0 \\ 0 & 0 & 0.0372 \end{bmatrix}$ [44]

and $\epsilon^0_{33} = 0.0372$ [44] to provide close fit to experimental length and aspect ratio time evolution data at the same temperature. Since temperature dependent misfit strain for Inconel 625 is lacking in the literature, these values were used for all temperature investigated in this study.

Values for the diffusion prefactor (D_0) and activation energy (Q) are needed to calculate the temperature dependent diffusivity of Al* and Nb*. Devaux *et al.* [43] reported that the growth of γ'' in Inconel 718 (a related derivative alloy) was controlled by volume diffusion of niobium in the matrix. Therefore, $Q_{Nb^*} = 295 kJmol^{-1}$ was calibrated to fit the phase-field results for isothermal aging at 650 °C to the linear region of the experimental γ'' length time evolution data since real time is calculated with Eq. (14) which requires D_{Nb^*} as input. The linear region of γ'' length time evolution curve represents the free diffusional growth of γ'' particles, with negligible elastic interaction or competition for solute between particles. Although it was observed that the diffusion of Al* had negligible effect on the growth kinetics of γ'', spurious negative concentration was observed in the γ'' phase during aging simulations at 650 °C. Therefore, $Q_{Al^*} = 325 kJmol^{-1}$ was chosen to avoid this. $D_0 = 8.8 \times 10^{-5} m^2/s$ [43] for both Al* and Nb*.

The interfacial energy is calibrated to obtain the maximum γ'' number density that would allow best fit of phase-field results to experimental γ'' morphological evolution data. The spatial nucleation probability (Eq. (11)) is extremely sensitive to the interfacial energy values because of the exponential terms in Eqs. (11) and (12). Therefore, the interfacial energy was carefully calibrated for isothermal aging at 600 °C ($\sigma = 172.88 mJ/m^2$) and 650 °C ($\sigma = 151.56 mJ/m^2$). See Fig. A1 in the Appendix for the effect of the interfacial energy on γ'' number density and morphological features. A linear fit is utilized for the temperature dependency of the interfacial energy between 600 °C to 760 °C temperature range investigated in this work. Table 3 compares the calibrated parameters used in this study to the values reported in the literature by different authors for γ'' in various alloy systems. It is important to note that apart from the composition and temperature dependency of material properties, the misfit strain and interfacial energy of γ'' are also dependent on the aspect ratio [46] and the degree of coherency [14], further adding to the difficulty of accurate characterization of these properties. A comprehensive list of all inputs used for the simulations is provided in Table 4.

After the calibration of the model parameters, phase-field simulations were performed at 600 °C and 650 °C aging temperatures with a grid size of 0.75 nm to investigate γ'' nucleation kinetics and morphology evolution. The 3D simulation volume size is $96 \times 96 \times 96 nm^3$. For each temperature, we performed five simulations with different random number generator seeds in order to capture the stochastic nature of nucleation. Furthermore, the results from the simulations were averaged to reduce the statistical errors associated with the relatively small

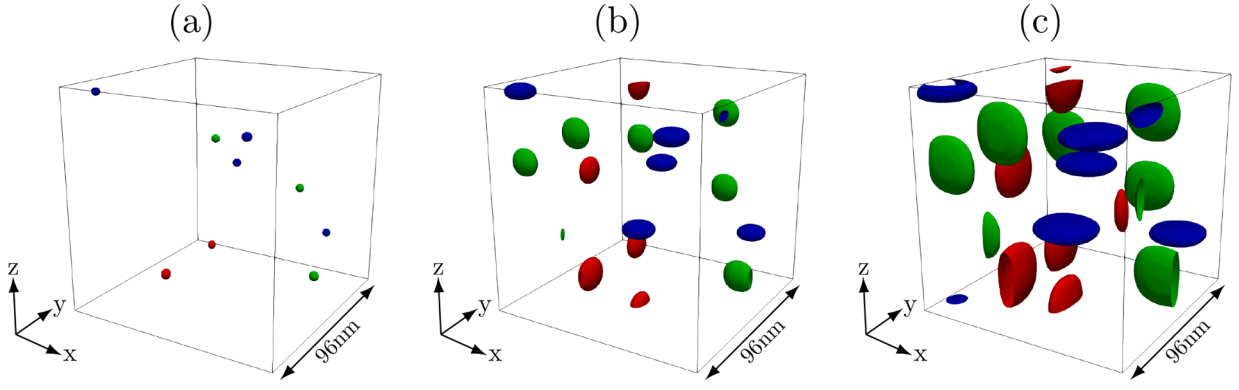

Fig. 3. Simulated microstructure evolution of γ'' precipitates in Inconel 625 aged at 600 °C. The phase-field simulations were performed in a $96 \times 96 \times 96 nm^3$ volume and are shown after aging for (a) 95 h, (b) 1185 h, and (c) 5405 h. The different colors represent different variants of γ''. The x-, y-, and z-axis represent [100], [010], and [001] directions, respectively.

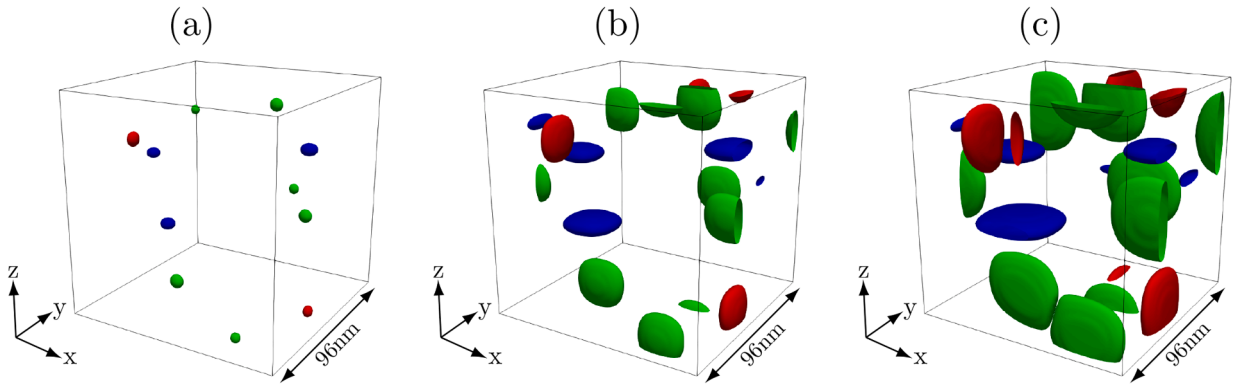

Fig. 4. Simulated microstructure evolution of γ″ precipitates in Inconel 625 aged at 650 °C. The phase-field simulations were performed in a $96 \times 96 \times 96\text{nm}^3$ volume and are shown after aging for (a) 10 h, (b) 105 h, and (c) 1000 h. The different colors represent different variants of γ″. The x-, y-, and z-axis represent [1 0 0], [0 1 0], and [0 0 1] directions, respectively.

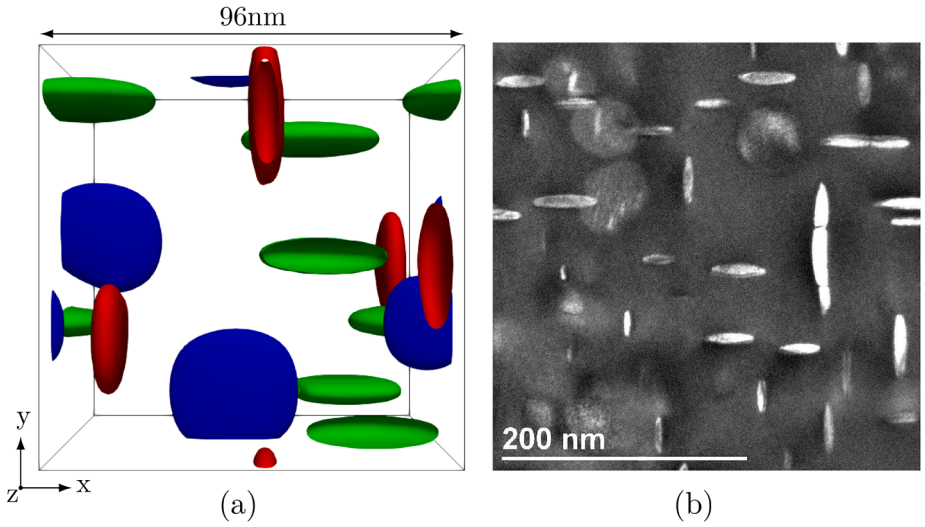

Fig. 5. Microstructure of γ″ precipitates in Inconel 625 aged at 650 °C for 1000 h. (a) Phase-filed simulation (b) TEM image with a [0 0 1] crystallographic orientation [8]. The different colors represent different variants of γ″. The x-, y-, and z-axis represent [1 0 0], [0 1 0], and [0 0 1] directions, respectively.

simulation volume size.

3. Results and discussion

3.1. Phase-field simulations: γ″ morphology evolution and kinetics

To obtain the morphological features of γ″ from the phase-field simulations, the precipitates were identified as regions with $|\eta_p| \geq 0.5$ and all 3D simulation images presented are contour plots of $|\eta_p| = 0.5$. The length of each γ″ variant is calculated from the radius of a circle fitted to each precipitate in their respective habit planes, {1 0 0}. The thickness is calculated along the distance perpendicular to the habit planes. The aspect ratio is defined as the thickness/length. And the

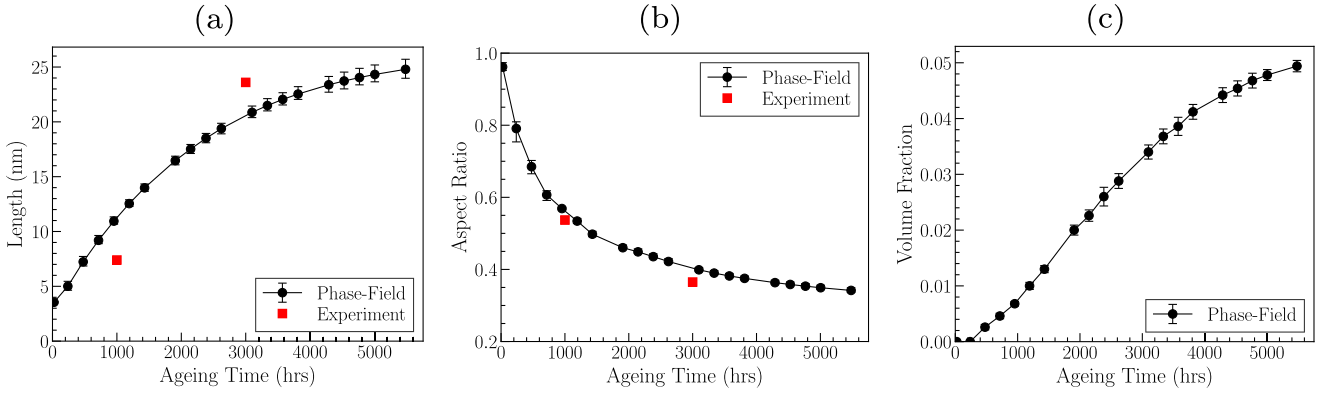

Fig. 6. Simulated γ″ precipitation kinetics in Inconel 625 aged at 600 °C and comparison with experimental measurements [46]. (a) Particle length. (b) Aspect ratio. (c) Volume fraction.

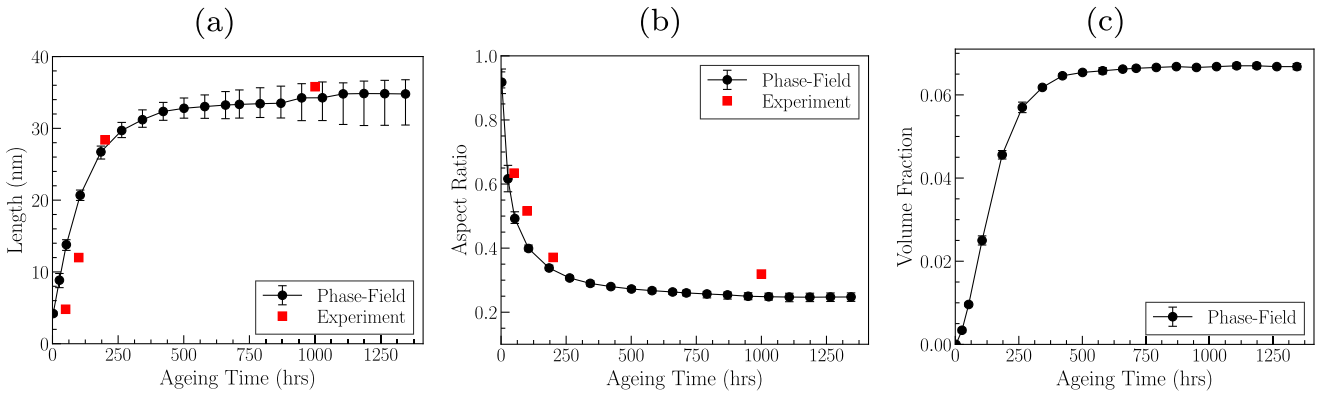

Fig. 7. Simulated γ'' precipitation kinetics in Inconel 625 aged at 650 °C and comparison with experimental measurements [46]. (a) Particle length. (b) Aspect ratio. (c) Volume fraction.

volume fraction was calculated as the fraction of nodes occupied by precipitates in the 3D simulation volume ($|\eta_p| \geq 0.5$). Fig. 3 and Fig. 4 illustrate the simulated γ'' precipitate morphological evolution for isothermal aging at 600 °C and 650 °C. From these figures, it is evident that the time evolution of γ'' into a disk-shaped morphology are well reconstructed by the phase-field simulations. Since the habit planes of γ'' are {1 0 0} planes, the major axis of the three variants (as indicated by the different colors) are perpendicular to one another. The simulated microstructure and experimental TEM image (Fig. 5) show that γ'' precipitates coalesced with each other along their edges except for those in antiphase relationships that align and attach to each other along their edges, leaving antiphase boundaries (APBs) in between. No face-to-face coalescence was observed because of elastic interactions among precipitates.

Fig. 6 and Fig. 7 show the evolution of mean particle length, aspect ratio (thickness/length), and volume fraction calculated from the phase-field simulations. The mean particle length, aspect ratio, and volume fraction were calculated from the aggregate of all particles from the five simulations with different random seeds. The error bars in the length and aspect ratio indicate the first and third quartiles of the distribution and the error bars in the volume fraction was calculated from the standard deviation between the five simulations. Generally, the simulated precipitate length and aspect ratio agree well with the experimental measurements. Deviations between the phase-field and experimental results occurred mainly in the early aging stages at both temperatures possibly because of the large critical nuclei size imposed on the nucleating particles (see section 3.2 for more details). Note that, although γ'' precipitates were assumed to nucleate as spherical particles, because of the anisotropic misfit strain tensor between γ'' and γ matrix, the growth of the particles along the major axis is faster than the growth along the minor axis. Consequently, the aspect ratio (thickness/length) decreases with aging time at a faster rate during the early growth stages compared to the later growth stages (Fig. 6b and Fig. 7b). While the current model utilizing an isotropic interfacial energy and isotropic interface kinetics offers favorable results compared to experimental morphological data, it should be noted that a tetragonal to cubic interface might exhibit strong anisotropic properties [18,20], which could also be incorporated in the phase-field model to improve the accuracy of the predicted morphological features [20]. To the best of our knowledge, no information about the magnitudes of such anisotropies for the γ/γ'' interface is available in the open literature. Therefore, we assume isotropic interfacial properties.

The volume fraction increases monotonically at the early aging stages for both temperatures (Fig. 6c and Fig. 7c). This is due to the free diffusional growth of the nucleated γ'' precipitates in the supersaturated γ matrix. The volume fraction reaches a saturation level as the supersaturation in the matrix decreases and elastic interaction alongside

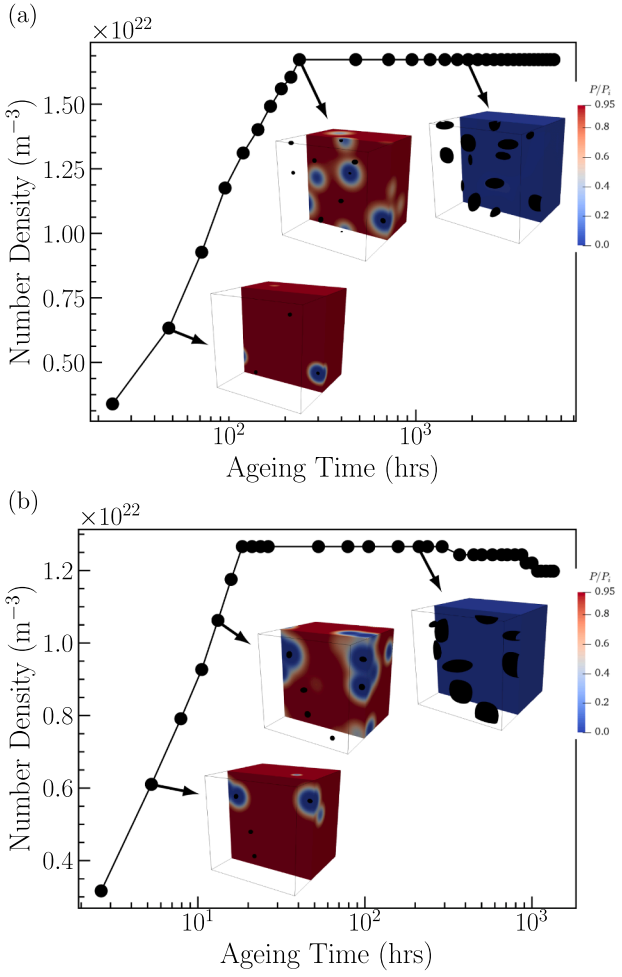

Fig. 8. Simulated γ'' number density evolution for aging at (a) 600 °C (b) 650 °C. The contour plot inserts indicate the spatial distribution of nucleation probability (P) relative to the initial nucleation probability (P_i). The red regions indicate high nucleation probability and the blue regions indicate low nucleation probability. γ'' particles are indicated by black spots.

competition for solute between particles arises. This is more pronounced for aging simulation at 650 °C (Fig. 7c) were the saturation volume fraction is about 6.7%. For aging simulation at 600 °C, the saturation volume fraction is not reached even after 5480 h of aging reported here. For comparison, the volume fraction calculated from the

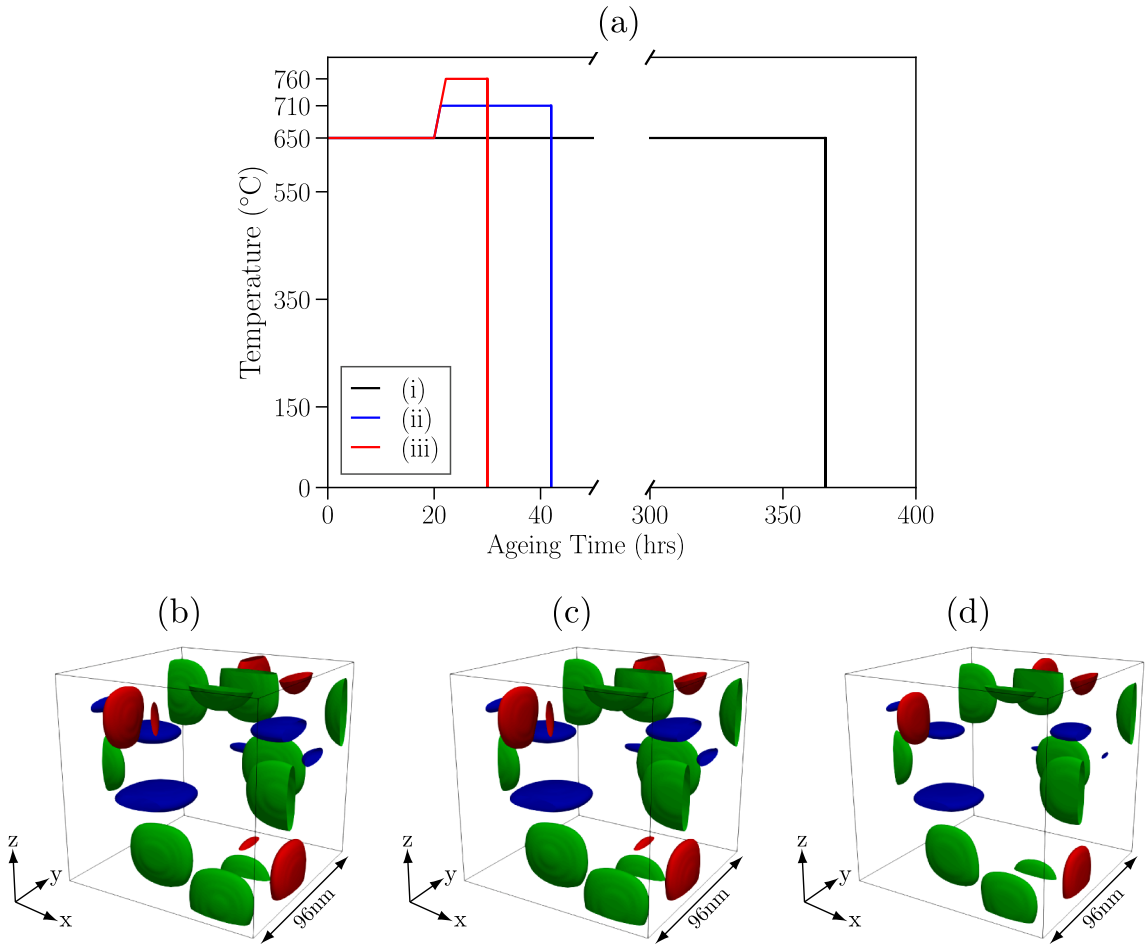

Fig. 9. (a) Various heat treatment schemes studied: (i) isothermal aging at 650 °C for 366 h; (ii) isothermal aging at 710 °C for 22 h after nucleation treatment at 650 °C for 20 h; (iii) isothermal aging at 760 °C for 10 h after nucleation treatment at 650 °C for 20 h (b), (c), (d) are the simulated microstructure evolution of γ'' precipitates in Inconel 625 for the various heat treatment schemes (i), (ii), and (iii), respectively. The phase-field simulations were performed in a $96 \times 96 \times 96\text{nm}^3$ volume. The different colors represent different variants of γ''. The x-, y-, and z-axis represent [100], [010], and [001] directions, respectively.

thermodynamic database is 10.1% at 650 °C [25] which is higher than the result from the phase-field simulation (6.7%). The reason for this deviation can be attributed to the fact that the phase-field model includes the contribution from both the interfacial and misfit strain energies which are not included in the calculation from the thermodynamic database that only considers the bulk free energies of the phases. Besides, the thermodynamic calculations report results as time goes to infinity.

3.2. *Phase-field simulations: γ'' nucleation kinetics*

The nucleation kinetics controls the number and spatial location of γ'' nuclei introduced into the simulation volume in each time step according to the probability of nucleation (P) calculated form Eq. (11). To determine numerically whether a particle nucleate locally or not within each time step, a random number is generated for each untransformed cell and nucleation occurs when the number is smaller than P. Fig. 8 shows the number density evolution for aging at 600 °C and 650 °C along with contour plot inserts showing the local nucleation probability (P) normalized by initial nucleation probability (P_i). As particles nucleate, their growth results in the depletion of Nb* concentration in the surrounding matrix, resulting in spatially uneven nucleation rates and lower nucleation probability around the particles. From the contour plot inserts in Fig. 8, the lower probability of nucleation around growing particles due to low local supersaturation can be observed. Also, as the growth of nucleated particles persists, a maximum number density is reached, and nucleation shuts off due to soft impingement. The maximum number density for aging at 600 °C (1.67×10^{22} m^{-3}) is greater than that for ageing at 650 °C (1.27×10^{22} m^{-3}). However, the nucleation rate at 650 °C is greater than at 600 °C as it takes 19 h to reach the maximum number density at 650 °C compared to 238 h at 600 °C. Although, the shrinkage of smaller particles as a result of Ostwald ripening was observed for all cases, the complete dissolution of the shrinking particles was not captured in the time interval simulated for aging at 600 °C and 650 °C. The reduction in number density for aging simulation at 650 °C in Fig. 8b is due to the coalescence of γ'' particles belonging to the same antiphase domain.

One of the challenges with simulating nucleation events in the phase-field method is that the simulation grid size needs to be small enough to resolve the critical nuclei radius (r). This presents a computationally expensive challenge, given that real time is directly proportional to grid size squared (Eq. (14)). Using the expressions in Table 2, the calculated critical nuclei radii (r) was about 0.6 nm for both isothermal aging at 600 °C and 650 °C. Since, the critical radius must be resolved by three grid sizes to ensure that the nucleating particles are stable in the current system, the simulation grid size would have to be about 0.2 nm, compared to the 0.75 nm used in this study. However, reducing the grid size to 0.2 nm would severely affect the real time step of the simulation (Eq. (14)). Also, more numerical grid points would be required to simulate the same physical volume. As a result, the computational effort

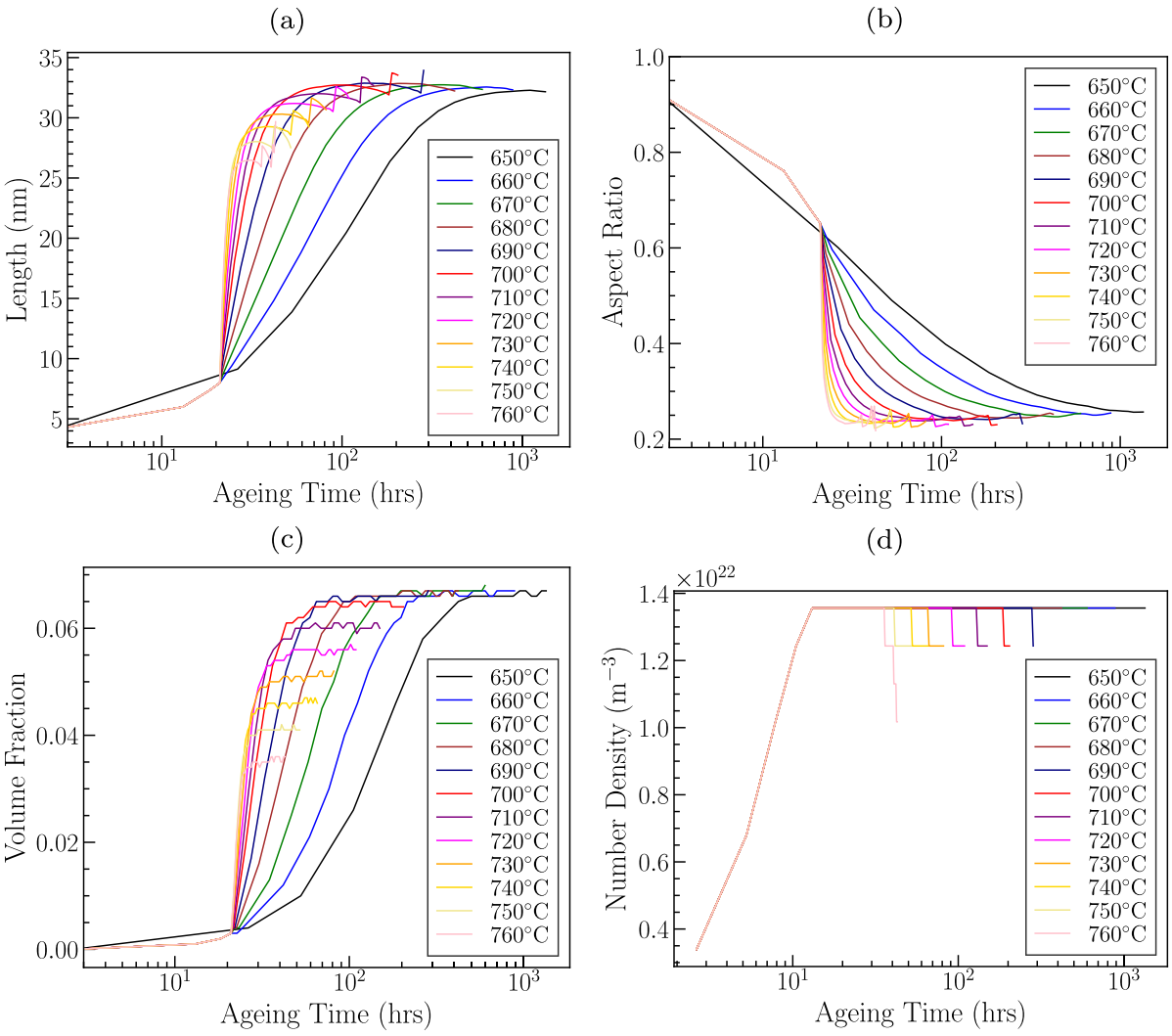

Fig. 10. Simulated γ'' precipitation kinetics in Inconel 625 after 20 h of nucleation treatment at 650 °C and subsequent aging at different temperatures. (a) Particle length. (b) Aspect ratio. (c) Volume fraction. (d) Number density.

would increase drastically. With this knowledge, we decided against reduction of grid size in order to capture the long aging times of Inconel 625.

3.3. Multistage aging strategy

Inconel 625 was originally designed as a solid-solution strengthened alloy [1], but precipitation hardening provided by the formation of γ'' secondary phase has been discovered to about double the yield strength of the alloy, albeit for a strict temperature range (550–750 °C) and uneconomical aging time (hundreds or even thousands of hours) [1,6,7,47]. Eiselstein *et al.* [1] cited this intermediate-temperature and sluggish aging response, as the major drawback of Inconel 625 compared to its counterpart Inconel 718. To this end, researchers have investigated possible means of decreasing the aging time of Inconel 625. One possible solution is by changes in composition giving raise to the creation of Inconel 625 plus which combines the excellent corrosion resistance of Inconel 625 and age-hardening capability of Inconel 718 [48,49]. Another solution is by means of multistage heat treatment. For example, Eiselstein *et al.* [1] investigated a high temperature (760 °C/1hr) heat treatment followed by aging at intermediate temperatures (621–677 °C) to trigger the precipitation reaction and reduce the nucleation time. Although, the slow growth of γ'' still persists at the intermediate temperatures. In this section, we numerically explore a multistage low-to-high temperature heat treatments, where nucleation at intermediate temperature is followed by higher temperature aging to accelerate the growth of the precipitates, taking advantage of faster solute mobility at higher temperatures.

For the multistage aging, a nucleation treatment at 650 °C for 20 h was chosen to avoid the heterogeneous nucleation of γ'' at grain boundaries, twin boundaries, and dislocations as observed by [3,46,50,51] at higher temperatures. Also, the temperature 650 °C provides a reasonable incubation time of about 5 h [2]. And after 20 h, the maximum number density at 650 °C was achieved (Fig. 8b). After the nucleation treatment, aging was carried out at higher temperatures (650–760 °C), as illustrated in Fig. 9a. The temperature dependent diffusivities, mobilities, elastic constants, interfacial energy, and Gibbs free energy calculated from the thermodynamic database [25] was used for the multistate aging simulations. All other parameters are the same as listed in Table 4. It is worth noting that the current model does not account for heterogeneous nucleation behaviors. Heterogeneous nucleation can be considered in the model by either introducing a phenomenological heterogeneous nucleation factor to match the simulated nucleation number density with experimental observations [20], or by directly incorporating the microstructure features responsible for heterogeneous nucleation such as grain boundaries [52] and dislocations [53]. However, these investigations are beyond the scope of the current study and will be left for future work.

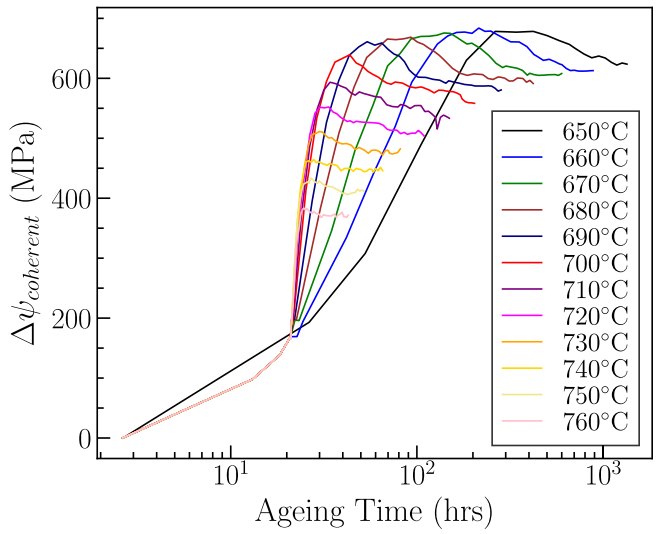

Fig. 11. Coherent strength evolution in Inconel 625 for multistage aging at different temperatures after a 20-hour nucleation treatment at 650 °C.

Fig. 9 shows the microstructure evolution for the aging performed at different temperatures after the nucleation treatment. Qualitative assessment of Fig. 9 shows that similar microstructure could be obtained if ageing is performed at higher temperatures and shorter times. For example aging at 710 °C for 22 h after nucleation treatment at 650 °C for 20 h (Fig. 9c) resulted in almost identical mean diameter and aspect ratio compared to isothermal aging at 650 °C for 366 h (Fig. 9b). Fig. 10 shows the evolution of the mean particle length, aspect ratio, volume fraction, and number density for aging at different temperatures after nucleation treatment at 650 °C. From Fig. 10, it is apparent that increasing aging temperature accelerates the growth and coarsening of γ'', albeit at the expense of the volume fraction and number density. This provides an avenue for decreasing the heat treatment time for Inconel 625 when the effect of reduced volume fraction and particle number density (lower coherent strength) is accounted for. The decrease in number density (Fig. 10d) is due to both the coalescence of γ'' particles belonging to the same antiphase domain and dissolution of smaller particles as a result of Ostwald ripening which is accelerated at elevated temperatures. The calculated mean length of the particles in the simulation volume increases as γ'' particles coalescence and smaller particles dissolve.

Table 5
Characterization of γ'' in Inconel 625 at the instance of maximum $\psi_{coherent}$. MS refer to the multistage aged samples.

Aging Temperature (°C)	Length (nm)	Thickness (nm)	Volume Fraction (%)	$\psi_{coherent}$ (MPa)	Total Aging Time (hrs)
650	31.3	8.8	6.5	678.3	421.8
690/MS	30.5	8.8	6.1	661.0	54.0
700/MS	30.8	8.5	6.1	639.3	43.6

3.4. γ'' coherent strengthening

The main purpose of alloy aging is to increase the strength of the material through precipitation hardening. The increase in yield strength as a result of the coherent strengthening effect of γ'' can be calculated as [54,55]:

$$\psi_{coherent} = 1.7MG|\epsilon|^{\frac{3}{2}}\left[\frac{h^2 f(1-\beta)}{2bR}\right]^{\frac{1}{2}} \tag{15}$$

where M is Taylor factor (3.06 for fcc materials), G is the shear modulus, ϵ is the tetragonal lattice misfit, f is the volume fraction of precipitates, R is the radius of the particles, h is the half thickness of the particles, β is a constant equals to $\frac{1}{3}$ when all the three variants are observed, and b is the magnitude of Burger's vector. We set $\epsilon = 0.0372$ [44], $G = 56$GPa, and $b = 2.56$Å [14]. R, h, and f are functions of aging time and were obtained from the phase-field simulations. Substituting all the values into Eq. (15), the coherent strengthening effect of γ'' as a function of aging time for both isothermal and multistage aging is calculated and plotted in Fig. 11. From the figure, it is apparent that coherent strengthening increases with aging time until a maximum value is reached, after which over-aging results in the decrease of coherent strengthening. For comparison, Eiselstein *et al.* [1] reported an increase in the yield strength at room temperature of about 525 MPa, for Inconel 625 samples isothermally aged at 650 °C for 1000 h while the present calculations reports an increase of 600.0 MPa for the same aging conditions.

To obtain the optimal multistage aging strategy, a cost/benefit analysis was performed by comparing the time required to reach the maximum strength at different multistage aging temperatures with the time required to reach the maximum strength for isothermal aging at 650 °C (678.3 MPa after 421.8 h). Fig. 12a shows the percent reduction in aging time and coherent strength loss as a function of aging

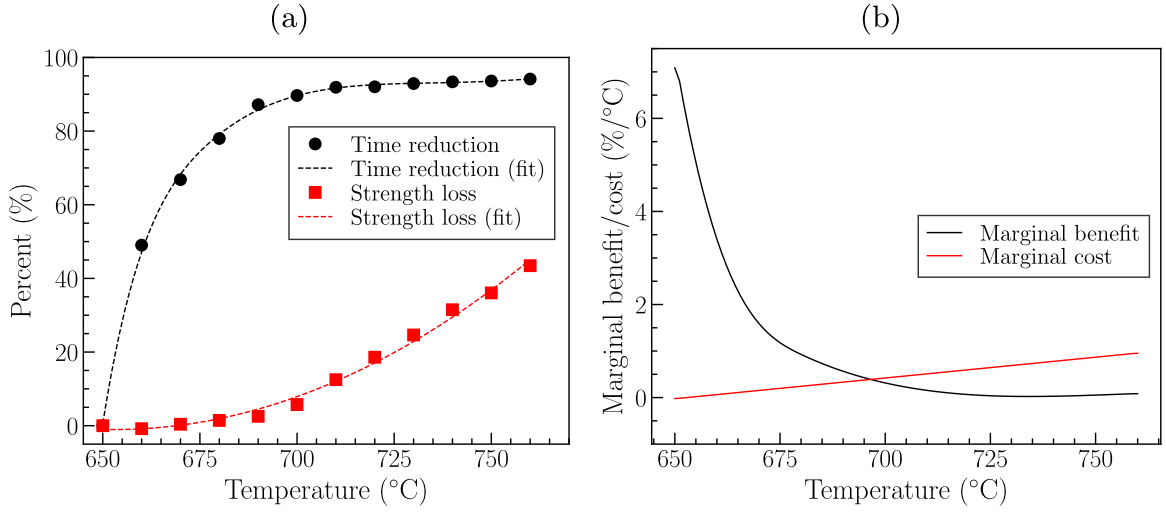

Fig. 12. Cost benefit analysis. (a) percent reduction in time and strength versus temperature (b) marginal benefit/cost versus temperature.

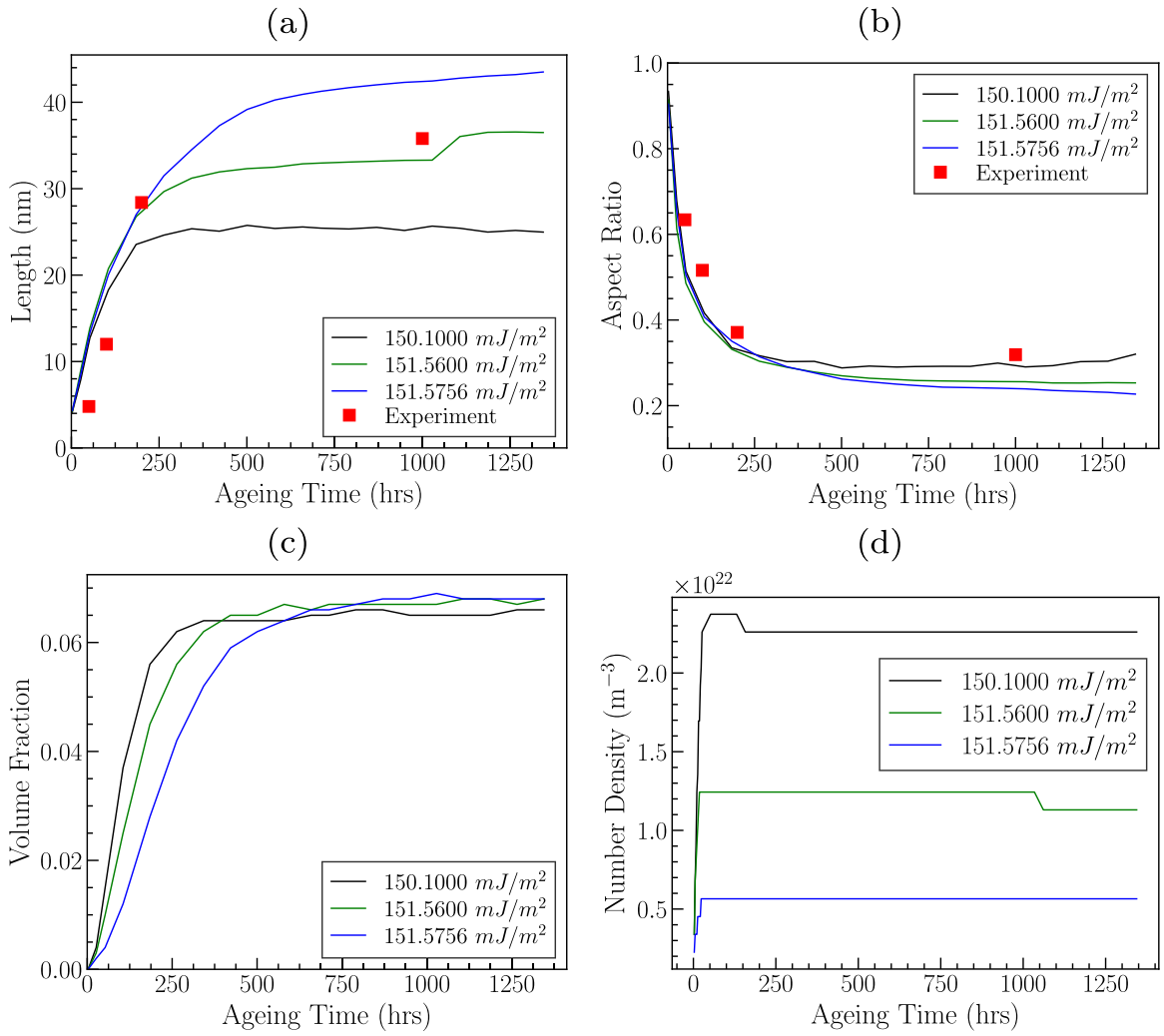

Fig. A1. Effect of interfacial energy on the Simulated γ″ precipitation kinetics in Inconel 625 aged at 650 °C and comparison with experimental measurements [46]. (a) Particle length. (b) Aspect ratio. (c) Volume fraction. (d) Number density.

temperature. Furthermore, defining the marginal benefit and marginal cost (Fig. 12b) as the slope of the time reduction and strength loss curves, respectively, an optimal aging temperature of 697 °C is obtained (intersect in Fig. 12b). Although simulation was not performed at 697 °C, it was observed that multistage aging at 690 °C resulted in time reduction of 87% with a strength loss of 2.6%. And multistage aging at 700 °C resulted in time reduction of 90% with a strength loss of 5.7%. The intersect in Fig. 12b is the point at which the ratio of the marginal benefit to marginal cost equals to unity. Aging at temperatures above this point would result in the ratio of the marginal benefit to marginal cost being less than unity. Meaning that any incremental benefit gained (time reduction) will result in a much higher incremental strength loss. For example, aging at 710 °C will reduce aging time by 91% but will result in a 12.5% strength loss. The properties of γ″ precipitates at the instance of maximum $\psi_{coherent}$ for isothermal aging at 650 °C along with multistage aging at 690 °C and 700 °C is detailed in Table 5.

4. Conclusions

In this study, we have developed a phase-field model to quantitatively investigate the γ″ nucleation and growth kinetics in Inconel 625 alloys and its coherency strengthening effect as a function of aging time and temperature. Using validated input parameters, our benchmark 3D simulations under isothermal conditions have well reproduced the experimentally observed γ″ morphology and precipitation kinetics. Due to the sluggish precipitation hardening response of Inconel 625, we have numerically explored multistage non-isothermal aging strategies to reduce aging time and applied an analytical strengthening model to predict the resulting precipitation hardening effect. Based on systematic analyses, we find that:

(1) Increasing the isothermal aging temperature during the multistage treatment would lead to reduction of γ″ number density and volume fraction, which further decreases the γ″ strengthening effect: the balance between strengthening effect and precipitation kinetics is critical for the design of heat treatment strategy.
(2) A 20-hour nucleation treatment at 650 °C followed by aging at 700 °C for 24 h can reduce the aging time by 90% with less than 6% loss of strength compared to isothermal aging at 650 °C for 422 h.
(3) A reliable phase-field model for process-structure–property predictions would require careful parameterization and calibration with benchmark experiments or theoretical analysis (see Section 2.6 for example), and identification and mitigation of possible sources of any deviations (see Section 3.2 for example). The current model will be further improved based on these discussions.

This work is expected to provide practical guidance to optimize the strength of Inconel 625 superalloy while significantly reducing the aging time, subject to experimental corroboration of the proposed multistage aging strategy. Also, the developed methodology can be applied to the design and process optimization of other materials systems during both isothermal and non-isothermal heat treatments.

CRediT authorship contribution statement

Caleb O. Yenusah: Conceptualization, Data curation, Formal analysis, Methodology, Software, Writing - original draft. **Yanzhou Ji:** Conceptualization, Formal analysis, Methodology, Software, Writing - original draft, Supervision. **Yucheng Liu:** Conceptualization, Funding acquisition, Investigation, Project administration, Supervision. **Tonya W. Stone:** Investigation. **Mark F. Horstemeyer:** Funding acquisition. **Long-Qing Chen:** Software. **Lei Chen:** Conceptualization, Funding acquisition, Investigation, Project administration, Supervision.

Declaration of Competing Interest

The authors declare that they have no known competing financial interests or personal relationships that could have appeared to influence the work reported in this paper.

Acknowledgements

This work is funded by the National Science Foundation (NSF), in United States under an award CMMI 1662854. The computer simulations were carried out on the clusters of High Performance Computing Collaboratory (HPC^2) at Mississippi State University. Lei Chen acknowledges the financial support by startup fund from Department of Mechanical Engineering at University of Michigan-Dearborn.

Data availability

The raw/processed data required to reproduce these findings cannot be shared at this time due to technical or time limitations.

Appendix A

The interfacial energy affects the nucleation barrier and therefore, the nucleation rate, nucleation probability, and maximum number density. A large interfacial energy value would lead to a slower nucleation rate, lower γ'' number density and slower growth kinetics. However, the mean length of the precipitates would be larger since there are fewer γ'' particles to compete for solute. Fig. A1 shows the effect of interfacial energy on the nucleation kinetics and morphological features of γ'' for phase-field simulations at 650 ℃ aging temperature. From the figure, $\sigma = 151.56 mJ/m^2$ was chosen for the simulation studies at 650 ℃ aging temperature in the main text of the manuscript. For $\sigma = 150.10 mJ/m^2$, the nucleation is much easier, resulting in a maximum number density of 2.37×10^{22} m^{-3}, a reduced mean length, and faster saturation of the precipitate volume fraction. For $\sigma = 151.5756 mJ/m^2$, the high nucleation barrier impedes the nucleation, resulting in maximum number density of 5.65×10^{21} m^{-3}, higher mean precipitate length, and a slower saturation of the precipitate volume fraction. The reduction in number density for $\sigma = 150.10 mJ/m^2$ and $\sigma = 151.56 mJ/m^2$ in Fig. A1 is due to the coalescence of γ'' particles belonging to the same antiphase domain. Although, the shrinkage of smaller particles as a result of Ostwald ripening was observed for all cases, the complete dissolution of the shrinking particles was not captured in the time interval simulated.

References

[1] H.L. Eiselstein, D.J. Tillack, The invention and definition of Alloy 625, Superalloys 718 (1991) 1–14.
[2] S. Floreen, G.E. Fuchs, W.J. Yang, The metallurgy of Alloy 625, Superalloys 718 (1994) 13–37.
[3] L.M. Suave, J. Cormier, P. Villechaise, A. Soula, Z. Hervier, D. Bertheau, J. Laigo, Microstructural evolutions during thermal aging of Alloy 625: impact of temperature and forming process, Metallurgical and materials transactions A 45 (2014) 2963–2982.
[4] X. Wang, P.W. Liu, Y. Ji, Y. Liu, M.H. Horstemeyer, L. Chen, Investigation on Microsegregation of IN718 Alloy During Additive Manufacturing via Integrated Phase-Field and Finite-Element Modeling, Journal of Materials Engineering and Performance 28 (2) (2019) 657–665.
[5] P. Liu, Z. Wang, Y. Xiao, R. Lebensohn, Y. Liu, M. Horstemeyer, X. Cui, L. Chen, Integration of phase-field model and crystal plasticity for the prediction of process-structure-property relation of additively manufactured metallic materials, International Journal of Plasticity 128 (2020), 102670.
[6] J.F. Radavich, A. Fort, Effects of long-time exposure in Alloy 625 at 1200 °F, 1400 °F and 1600 °F, Superalloys 718 (1994) 635–647.
[7] C. R. Conder, G. D. Smith and J. F. Radavich, "Microstructural and mechanical property characterization of aged Inconel alloy 625LCF," Superalloys 718, 625, 706 and various derivatives, pp. 447-458, 1997.
[8] I.J. Moore, M.G. Burke, E.J. Palmiere, Modelling the nucleation, growth and coarsening kinetics of γ" ($D0_{22}$) precipitates in the Ni-base Alloy 625, Acta Materialia 119 (2016) 157–166.
[9] I.J. Moore, M.G. Burke, N.T. Nuhfer, E.J. Palmiere, Evaluation of classical precipitation descriptions for in γ" (Ni_3Nb-$D0_{22}$) Ni-base superalloys, Journal of Materials Science 52 (2017) 8665–8680.
[10] L.-Q. Chen, Phase-Field Models for Microstructure Evolution, Annu. Rev. Mater. Res. 32 (1) (2002) 113–140.
[11] J.Z. Zhu, Z.K. Liu, V. Vaithyanathan, L.Q. Chen, Linking phase-field model to CALPHAD: application to precipitate shape evolution in Ni-base alloys, Scripta Materialia 46 (5) (2002) 401–406.
[12] J.Z. Zhu, T. Wang, A.J. Ardell, S.H. Zhou, Z.K. Liu, L.Q. Chen, Three-dimensional phase-field simulations of coarsening kinetics of γ' particles in binary Ni–Al alloys, Acta materialia 52 (2004) 2837–2845.
[13] N. Zhou, D.C. Lv, H.L. Zhang, D. McAllister, F. Zhang, M.J. Mills, Y. Wang, Computer simulation of phase transformation and plastic deformation in IN718 superalloy: Microstructural evolution during precipitation, Acta Materialia 65 (2014) 270–286.
[14] Y. Ji, Y. Lou, M. Qu, J.D. Rowatt, F. Zhang, T.W. Simpson, L.-Q. Chen, Predicting Coherency Loss of γ" Precipitates in IN718 Superalloy, Metallurgical and Materials Transactions A 47 (2016) 3235–3247.
[15] Y. Gao, H. Liu, R. Shi, N. Zhou, Z. Xu, Y.M. Zhu, J.F. Nie, Y. Wang, Simulation study of precipitation in an Mg–Y–Nd alloy, Acta Materialia 60 (2012) 4819–4832.
[16] H. Liu, Y. Gao, J.Z. Liu, Y.M. Zhu, Y. Wang, J.F. Nie, A simulation study of the shape of β′ precipitates in Mg–Y and Mg–Gd alloys, Acta Materialia 61 (2) (2013) 453–466.
[17] Y.Z. Ji, A. Issa, T.W. Heo, J.E. Saal, C. Wolverton, L.-Q. Chen, Predicting β′ precipitate morphology and evolution in Mg–RE alloys using a combination of first-principles calculations and phase-field modeling, Acta Materialia 76 (2014) 259–271.
[18] V. Vaithyanathan, C. Wolverton, L.Q. Chen, Multiscale modeling of θ' precipitation in Al–Cu binary alloys, Acta Materialia 52 (2004) 2973–2987.
[19] S.Y. Hu, J. Murray, H. Weiland, Z.K. Liu, L.Q. Chen, Thermodynamic description and growth kinetics of stoichiometric precipitates in the phase-field approach, Calphad 31 (2) (2007) 303–312.
[20] Y. Ji, B. Ghaffari, M. Li, L.-Q. Chen, Phase-field modeling of θ′ precipitation kinetics in 319 aluminum alloys, Computational Materials Science 151 (2018) 84–94.
[21] R. Shi, N. Ma, Y. Wang, Predicting equilibrium shape of precipitates as function of coherency state, Acta Materialia 60 (2012) 4172–4184.
[22] M. Asle Zaeem, H. El Kadiri, M.F. Horstemeyer, M. Khafizov, Z. Utegulov, Effects of internal stresses and intermediate phases on the coarsening of coherent precipitates: A phase-field study, Current Applied Physics 12 (2) (2012) 570–580.
[23] M. Asle Zaeem, H. El Kadiri, S.D. Mesarovic, M.F. Horstemeyer, P.T. Wang, Effect of the Compositional Strain on the Diffusive Interface Thickness and on the Phase Transformation in a Phase-Field Model for Binary Alloys, Journal of Phase Equilibria and Diffusion 32 (4) (2011) 302–308.
[24] R. Shi, D.P. McAllister, N. Zhou, A.J. Detor, R. DiDomizio, M.J. Mills, Y. Wang, Growth behavior of γ'/γ" coprecipitates in Ni-Base superalloys, Acta Materialia 164 (2019) 220–236.
[25] F. Zhang, "Ni-Nb-Al pseudo-ternary thermodynamic database," Madison, 2010.
[26] M. Yang, H. Wei, J. Zhang, Y. Zhao, T. Jin, L. Liu, X.F. Sun, Phase-field study on effects of antiphase domain and elastic energy on evolution of γ′ precipitates in nickel-based superalloys, Computational Materials Science 129 (2017) 211–219.

[27] S.G. Kim, W.T. Kim, T. Suzuki, Phase-field model for binary alloys, Phys. Rev. E 60 (6) (1999) 7186–7197.
[28] A.A. Wheeler, W.J. Boettinger, G.B. McFadden, Phase-field model of solute trapping during solidification, Phys. Rev. E 47 (3) (1993) 1893–1909.
[29] A.A. Wheeler, W.J. Boettinger, G.B. McFadden, Phase-field model for isothermal phase transitions in binary alloys, Phys. Rev. A 45 (10) (1992) 7424–7439.
[30] A. G. Khachaturyan, "Theory of structural transformation in solids," 1983.
[31] F. Schleifer, M. Holzinger, Y.Y. Lin, U. Glatzel, M. Fleck, Phase-field modeling of γ/γ" microstructure formation in Ni-based superalloys with high γ" volume fraction, Intermetallics 120 (2020), 106745.
[32] J.P. Simmons, C. Shen, Y. Wang, Phase field modeling of simultaneous nucleation and growth by explicitly incorporating nucleation events, Scripta Materialia 43 (10) (2000) 935–942.
[33] J.P. Simmons, Y. Wen, C. Shen, Y.Z. Wang, Microstructural development involving nucleation and growth phenomena simulated with the Phase Field method, Materials Science and Engineering: A 365 (1-2) (2004) 136–143.
[34] M. Avrami, Kinetics of phase change. I General theory, The Journal of chemical physics 7 (12) (1939) 1103–1112.
[35] M. Avrami, Kinetics of Phase Change. II Transformation-Time Relations for Random Distribution of Nuclei, The Journal of Chemical Physics 8 (2) (1940) 212–224.
[36] M. Avrami, Granulation, Phase Change, and Microstructure Kinetics of Phase Change. III, The Journal of Chemical Physics 9 (2) (1941) 177–184.
[37] A.M. Jokisaari, C. Permann, K. Thornton, A nucleation algorithm for the coupled conserved–nonconserved phase field model, Computational Materials Science 112 (2016) 128–138.
[38] S.M. Allen, J.W. Cahn, A microscopic theory for antiphase boundary motion and its application to antiphase domain coarsening, Acta metallurgica 27 (1979) 1085–1095.
[39] L.Q. Chen, J. Shen, Applications of semi-implicit Fourier-spectral method to phase field equations, Computer Physics Communications 108 (2-3) (1998) 147–158.
[40] Z. Wang, A.D. Stoica, D. Ma, A.M. Beese, Diffraction and single-crystal elastic constants of Inconel 625 at room and elevated temperatures determined by neutron diffraction, Materials Science and Engineering: A 674 (2016) 406–412.
[41] R. Lawitzki, S. Hassan, L. Karge, J. Wagner, D. Wang, J. von Kobylinski, C. Krempaszky, M. Hofmann, R. Gilles, G. Schmitz, Differentiation of γ′- and γ″-precipitates in Inconel 718 by a complementary study with small-angle neutron scattering and analytical microscopy, Acta Materialia 163 (2019) 28–39.
[42] C. Slama, C. Servant, G. Cizeron, Aging of the Inconel 718 alloy between 500 and 750 °C, Journal of materials research 12 (1997) 2298–2316.
[43] A. Devaux, L. Nazé, R. Molins, A. Pineau, A. Organista, J.Y. Guédou, J.F. Uginet, P. Héritier, Gamma double prime precipitation kinetic in Alloy 718, Materials Science and Engineering: A 486 (1-2) (2008) 117–122.
[44] R. Cozar, A. Pineau, Influence of coherency strains on precipitate shape in a Fe Ni Ta alloy, Scripta Metallurgica 7 (8) (1973) 851–854.
[45] R.Y. Zhang, H.L. Qin, Z.N. Bi, J. Li, S. Paul, T.L. Lee, S.Y. Zhang, J. Zhang, H. B. Dong, Temperature-Dependent Misfit Stress in Gamma Double Prime Strengthened Ni-Base Superalloys, Metallurgical and Materials Transactions A 51 (4) (2020) 1860–1873.
[46] I. J. Moore, Modelling γ" (D022) precipitate nucleation, growth and coarsening in the nickel-base superalloy 625, PhD thesis: University of Sheffield, 2017.
[47] L.M. Suave, D. Bertheau, J. Cormier, P. Villechaise, A. Soula, Z. Hervier, J. Laigo, J. Y. Guédou, J. Choné, Impact of microstructural evolutions during thermal aging of Alloy 625 on its monotonic mechanical properties, MATEC Web of Conferences 14 (2014) 21001, https://doi.org/10.1051/matecconf/20141421001.
[48] N.B. Schmidt, T.A. DeBold, R.B. Frank, Custom age 625® plus alloy—A higher strength alternative to alloy 625, Journal of Materials Engineering and Performance 1 (4) (1992) 483–488.
[49] L.-J. Yu, E.A. Marquis, Precipitation behavior of Alloy 625 and Alloy 625 plus, Journal of Alloys and Compounds 811 (2019), 151916.
[50] M. Sundararaman and P. Mukhopadhyay, "Heterogeneous Precipitation of the γ" Phase in Inconel 625," Materials Science Forum, vol. 3, pp. 273-280, 1985.
[51] M. Sundararaman, R. Kishore and P. Mukhopadhyay, "Some aspects of the heterogeneous precipitation of the metastable γ" phase in Alloy 625," Superalloys 718, 625, 706 and various derivatives, pp. 405-418, 1994.
[52] R. Shi, T.W. Heo, B.C. Wood, Y. Wang, Critical nuclei at hetero-phase interfaces, Acta Materialia 200 (2020) 510–525.
[53] H. Liu, Y. Gao, Y.M. Zhu, Y. Wang, J.F. Nie, A simulation study of β1 precipitation on dislocations in an Mg–rare earth alloy, Acta Materialia 77 (2014) 133–150.
[54] J.M. Oblak, D.F. Paulonis, D.S. Duvall, Coherency strengthening in Ni base alloys hardened by $D0_{22}$ γ" precipitates, Metallurgical Transactions 5 (1974) 143.
[55] J.M. Oblak, D.S. Duvall, D.F. Paulonis, An estimate of the strengthening arising from coherent, tetragonally-distorted particles, Materials Science and Engineering 13 (1) (1974) 51–56.
[56] E. Kozeschnik, I. Holzer, B. Sonderegger, On the Potential for Improving Equilibrium Thermodynamic Databases with Kinetic Simulations, Journal of Phase Equilibria and Diffusion 28 (1) (2007) 64–71.